npj | 2D materials and applications

www.nature.com/npj2dmaterials

ARTICLE OPEN

Check for updates

Electron irradiation-induced defects for reliability improvement in monolayer MoS_2-based conductive-point memory devices

Xiaohan Wu[1,2], Yuqian Gu[1,2], Ruijing Ge[1], Martha I. Serna[1], Yifu Huang[1], Jack C. Lee[1]✉ and Deji Akinwande[1]✉

Monolayer molybdenum disulfide has been previously discovered to exhibit non-volatile resistive switching behavior in a vertical metal-insulator-metal structure, featuring ultra-thin sub-nanometer active layer thickness. However, the reliability of these nascent 2D-based memory devices was not previously investigated for practical applications. Here, we employ an electron irradiation treatment on monolayer MoS_2 film to modify the defect properties. Raman, photoluminescence, and X-ray photoelectron spectroscopy measurements have been performed to confirm the increasing amount of sulfur vacancies introduced by the e-beam irradiation process. The statistical electrical studies reveal the reliability can be improved by up to 1.5× for yield and 11× for average DC cycling endurance in the devices with a moderate radiation dose compared to unirradiated devices. Based on our previously proposed virtual conductive-point model with the metal ion substitution into sulfur vacancy, Monte Carlo simulations have been performed to illustrate the irradiation effect on device reliability, elucidating a clustering failure mechanism. This work provides an approach by electron irradiation to enhance the reliability of 2D memory devices and inspires further research in defect engineering to precisely control the switching properties for a wide range of applications from memory computing to radio-frequency switches.

npj 2D Materials and Applications (2022)6:31 ; https://doi.org/10.1038/s41699-022-00306-8

INTRODUCTION

As an emerging material system, two-dimensional (2D) material has attracted much attention in the last two decades due to its unique electronic, optical, mechanical and thermal properties[1–4]. Since the realization of graphene, a large number of materials in this category has been uncovered, including transitional metal dichalcogenides (TMDs), hexagonal boron nitride (h-BN), and graphene-like Xenes (X refers to elements ranging from group III to group VI)[5–11]. The 2D atomic sheets are defined as atomically thin, layered solids with intralayer covalent bonding and interlayer van der Waals bonding, representing the thinnest unsupported crystalline that can be realized[7,12]. Graphene has been utilized in electronic devices mainly as the conducting materials since it is a zero-gap semiconductor, with a remarkable electron mobility in excess of 15,000 $cm^2 V^{-1} s^{-1}$ at room temperature in clean samples[5,13]. Molybdenum disulfide (MoS_2), a representative TMD material, has a ~1.8 eV direct band gap in monolayer form, thus is suitable to be used in opto-electronic devices or as the channel material in field-effect transistors[3,12,14,15]. In addition, h-BN, a 2D insulator, has a large band gap of ~5.9 eV, which has been used extensively as a dielectric or substrate material, or to form heterostructures with other 2D materials in flexible devices[10,16,17]. With the collection of 2D materials rapidly expanded to several hundreds, featuring diverse properties, the semiconductor industry is expected to be boosted by these emerging materials[18].

Among various applications, memory devices have been regarded as the technology driver in the recent years[19,20]. Non-volatile resistive switching (NVRS) devices, also known as memristors, stand out as a promising candidate as the next-generation non-volatile memory[21–23]. The operation of NVRS devices is based on the resistive switching phenomenon of the active layer, typically a bulk metal-oxide film, such as SiO_2 or HfO_2, in a metal-insulator-metal (MIM) stacking structure[24–27]. By applying external electrical bias, the device can be repeatably switched between a high-resistance state and a low-resistance state, which can be subsequently sustained without power supply.

In the last few years, various 2D materials have been reported to exhibit NVRS phenomenon, expanding to a broad collection of the ultrathin layered crystalline films[28]. As a zero-gap semiconductor, graphene may not be suitable as the resistive switching layer. Graphene oxide, on the other hand, has been reported to show NVRS phenomenon in memory devices[29–31]. MoS_2, the most studied semiconducting 2D material, has been found to show memristive effect in various forms, including 1T-phase nanosheets, solution-processed films, heterostructure with metal oxide, double-transferred layers and oxidized multi-layer MoS_2[32–39]. Other 2D materials, such as multi-layer h-BN or oxidized black phosphorus, have also been demonstrated to exhibit NVRS characteristics[40–42].

Resistive switching was not initially thought to be accessible in monolayer atomic sheets due to excessive leakage current[43]. Recently, researchers have found that grain boundaries in monolayer MoS_2 could produce NVRS behavior based on planar structure[44,45]. However, the vertical MIM devices are more favorable for practical integration with smaller footprint and 3D stacking capability. In 2018, it was firstly reported that monolayer chemical vapor deposition (CVD)-grown MoS_2, together with other TMDs ($MoSe_2$, WS_2, and WSe_2), shows intrinsic NVRS phenomenon in the desired vertical MIM configuration[46,47]. The demonstration of monolayer h-BN memristors further set the record for the thinnest material with NVRS to ~0.3 nm[48]. These devices can be collectively labelled as *atomristors* (memristive effect in atomically

[1]Microelectronics Research Center, The University of Texas at Austin, Austin, TX 78758, USA. [2]These authors contributed equally: Xiaohan Wu, Yuqian Gu.
✉email: leejc@austin.utexas.edu; deji@ece.utexas.edu

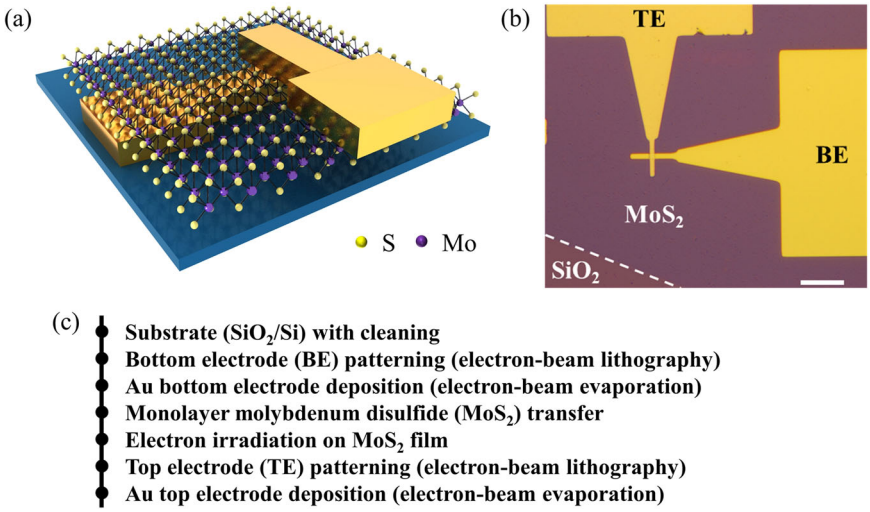

Fig. 1 Device structure and fabrication process. a The schematic and (**b**) optical image of metal-2D material-metal sandwich structure for crossbar devices. Scale bar represents 20 μm. The monolayer MoS_2 acts as the resistive switching layer. **c** The process flow of MoS_2-based NVRS crossbar devices featuring e-beam irradiation treatment.

thin sheets), featuring low switching voltages, large on/off ratio, fast switching speed, and forming-free characteristics. However, the 2D-based NVRS devices still face the challenges of relatively low yield and endurance. Our previous first-principles simulation study and atomic-scale scanning tunneling microscopy (STM) results indicate that the interaction between sulfur vacancies on MoS_2 film and metal ions from electrodes can result in the NVRS phenomenon[49,50]. In addition, a recent theoretical study proposed that the vacancy defect positions can be modulated by an electric field that can produce NVRS[51]. Thus, the defect properties in 2D materials are expected to play a significant role in the switching behavior.

Defects in MoS_2, such as vacancies, traps, and grain boundaries, can be introduced in material preparation or followed fabrication process[52,53]. These additional defects lead to mobility degradation compared to the theoretical predictions[54]. On the other hand, with further understanding of these defects, defect engineering is explored to modulate the properties of 2D materials, which enables some novel applications. For example, defects could act as carrier donors. MoS_2 can exhibit both n-type and p-type conduction with intrinsic defects[55]. While the intrinsic defects typically lead to n-type conduction in MoS_2, Nb-doping is found can effectively shift the Fermi level of MoS_2 and thus induce p-type doping MoS_2[56]. Near-Infrared Opto-electronic application can be achieved in MoS_2 with induced sulfur vacancies as well[57]. Chemically reactive defects can also be induced in MoS_2 with defect engineering, which can improve the catalyst efficiency of MoS_2 on hydrogen production[58]. For those reasons, defects engineering on 2D materials has been attracting much attention[59].

Electron-beam irradiation is well known as an experimental method to modulate the density of sulfur vacancies of CVD-grown or exfoliated MoS_2 sheets, affecting their chemically active defects[59–61]. These introduced defects typically deteriorate the MoS_2-based device quality in some applications, such as field-effect transistors. However, for NVRS devices, a certain amount of defects is desired to facilitate the formation of conductive paths in the active layer[25]. To the best of our knowledge, there has been no report to systematically employ the defect engineering in the application of 2D memristors. In this work, we firstly used the e-beam irradiation method on the ultra-thin monolayer MoS_2 NVRS devices and successfully improved the reliability significantly. The material characterizations including Raman and photoluminescence (PL) spectra indicate sulfur vacancies have been induced by the irradiation process. X-ray photoelectron spectroscopy (XPS) measurement further demonstrates the loss of sulfur after irradiation. The statistical electrical measurement results show that the reliability can be improved by up to 1.5× for yield and 11× for average DC cycling endurance compared with unirradiated devices, which can be explained by the increased amount of sulfur vacancies that promote the formation of (virtual) "conductive points" in monolayer MoS_2 films. However, under extremely high irradiation doses, the device performance has been found to degrade, showing low yield and endurance due to the excessive amount of sulfur vacancies. For the first time on 2D NVRS devices, Monte Carlo simulations have been performed to illustrate the effect of induced vacancies on the electrical characteristics. The results support the contention that electron irradiation treatment can be used to enhance the reliability of 2D-monolayer based NVRS devices and provide additional evidence for the conductive-point switching mechanisms through vacancies. This work provides additional insights into optimizing 2D-material devices with advanced defect engineering, and paves the way for practical applications in high-density neuromorphic computing, flexible non-volatile memory fabrics, and zero-power radio-frequency (RF) switches.

RESULTS

Sample preparation and device fabrication

The 2D NVRS devices are fabricated using continuous CVD-grown monolayer MoS_2 film sandwiched between Au top and bottom electrodes (BE) in the vertical MIM structure. We use the crossbar to define the active device area as the overlapped region between two electrodes. Figure 1a, b show the schematic and optical image of the MoS_2 NVRS devices, respectively. The active layer thickness is only 0.7 nm for the monolayer MoS_2, highlighting the breakthrough of the memristive effect into atomically thin materials. The inert metal, gold, is used as electrode material to eliminate possible effect of metal oxides at the metal-2D material interface[46]. The fabrication process is illustrated in Fig. 1c. After MoS_2 transferring, the film is irradiated by electron beam in a Raith eLINE lithography system with various radiation doses up to 10^5 μC/cm^2. Our previous studies have demonstrated that the resistive switching phenomenon in the fabricated 2D devices is intrinsically originated from the MoS_2 monolayer. The potential parasitic effect from the MoS_2 outside of the device area can be excluded by the thermal release tape transfer device showing similar NVRS

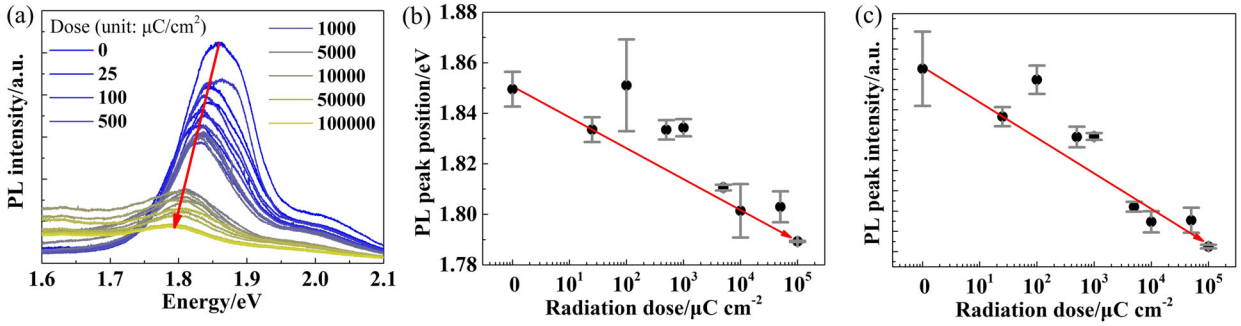

Fig. 2 Photoluminescence (PL) spectra analysis of the irradiation effect on monolayer MoS_2. a The PL spectra of monolayer MoS_2 with different radiation doses up to 10^5 μC/cm^2. The peak for unirradiated sample at ~1.85 eV is consistent with previous reports for monolayer MoS_2. **b** The relationship between PL peak position and radiation dose. A red shift can be observed as dose increases. **c** The relationship between PL peak intensity and radiation dose. A decrease of peak intensity can be observed as dose increases. These suggest sulfur vacancies are introduced to the MoS_2 film after irradiation. The PL spectra are measured on three different locations for each dose to compensate for variation from material growth.

phenomenon in Supplementary Fig. 1. The difference in film properties caused by the electron irradiation process is expected to toggle the switching performance. Note that the TE e-beam lithography process may have certain portion of electrons penetrating through the resist[62,63]. However, these electrons are applied equally to all the exposed regions and devices. Thus, it can be regarded as an identical offset to all doses and does not influence the trends in the following analysis.

Characterization of monolayer MoS_2 after irradiation

Material characterizations, PL and Raman spectroscopy, have been conducted on the samples to evaluate the monolayer MoS_2 after irradiation. Normally the PL and Raman data were measured on three different locations for each radiation dose for confidence and accuracy on the variation of signals per evaluated area. Irradiation doses in two different range of interest are investigated with two monolayer MoS_2 samples on different batches. Figure 2a and Supplementary Fig. 2a show the PL of the monolayer MoS_2 sample with different radiation doses. The PL peak position for unirradiated MoS_2 is located at ~1.85 eV, in good agreement with the reported optical band gap[64]. Two major trends, showing a red shift of peak position and a decrease of peak intensity as dose increases, are shown in Fig. 2b, c, respectively. The red shift of PL peak position is consistent with previous report on e-beam exposed monolayer MoS_2, which can be attributed to the sulfur vacancies generated by the electron irradiation process[65]. The decrease of intensity is believed to be due to defects generated in the mid-gap that modify the recombination process[66]. Note that the red shift of peaks cannot be observed in PL quenching associated with oxygen defect sites, indicating negligible oxygen defects introduced during the irradiation process[66].

In addition to PL measurement, Raman spectra of the monolayer MoS_2 films has been used to confirm and investigate defects induced by electron irradiation (Fig. 3a and Supplementary Fig. 2b). The two characteristic peaks for MoS_2, corresponding to the in-plane vibrational E_{2g} mode at ~386 cm^{-1} and the out-of-plane A_{1g} mode at 405 cm^{-1}. The frequency difference (~19 cm^{-1}) is in good agreement with the reported value, suggesting a high-quality uniform monolayer crystalline film[67]. As the irradiation dose increases, the intensity of E_{2g} and A_{1g} peaks decreases (Fig. 3b, c). The E_{2g} and A_{1g} peaks exposed with the dose of 10^5 μC/cm^2 have been found to be 16% and 23% lower than pristine monolayer MoS_2, respectively. A plausible mechanism is weakening of collective vibration due to the loss of atoms. This continual decrease in intensity of E_{2g} and A_{1g} peaks with increasing radiation dose is consistent with DFT prediction of Raman spectrum of MoS_2 supercell with single sulfur vacancy, and this is further confirmed by the disappearance of the 2LA(M) mode (Fig. 3d)[68]. As to the Raman peak positions, the E_{2g} peak and A_{1g} peak are observed to be red-shifted with increasing dose, as shown in Supplementary Fig. 3. The E_{2g} peak red shifts as restoring force constant of in-plane vibrations (E_{2g}) are weaken due to breakage of Mo–S bonds and generation of sulfur vacancies[69,70]. Supplementary Fig. 4 shows FWHM of both E_{2g} and A_{1g} peaks have an increasing trend with increasing radiation dose. The broadening reflects the degradation of crystallinity, due to generation of defects in MoS_2 with electron irradiation. Similar results from electron irradiation treatment, as reflected by Raman spectra, have been observed in exfoliated monolayer MoS_2, as shown in Supplementary Fig. 5. These results indicate that the additional defects are originated from electron irradiation treatment, and not native defects in the CVD-grown MoS_2 films. Based on these results, one can deduce that sulfur vacancies are introduced to the monolayer MoS_2 film by irradiation process.

Moreover, XPS measurement has been performed on the samples with e-beam irradiation treatment to confirm the change of composition in the material. Figure 4 shows the XPS results for the MoS_2 film with no irradiation, a dose of 250 μC cm^{-2}, and a dose of 5000 μC cm^{-2}, respectively. In Fig. 4a, binding energies of 230.1 eV (Mo $3d^{5/2}$), 233.2 eV (Mo $3d^{3/2}$), and 227.2 eV (S 2 s) were identified as MoS_2 characteristic peaks[71,72]. Also, the presence of superficial Mo^{6+} (233.1 eV and 236.3 eV) was observed (corresponding to MoO_3)[73]. Molybdenum oxide could be possibly due to air exposure before analysis or natively from the CVD-grown MoS_2. Also, in the sulfur 2p region (Fig. 4b), the peaks with binding energy at 162.9 eV and 164.1 eV were identified as part of the film. The Mo:S ratio is calculated to be 1:2.37, which is reasonable compared to the theoretical ratio of 1:2 considering the error or tolerance of XPS analysis. Figure 4c, d show the Mo 3d and S 2p region for XPS of the sample with the e-beam irradiation dose of 250 μC cm^{-2}. In addition to MoS_2 and MoO_3 identified in the unirradiated sample, peaks at 230.2 eV and 233.3 eV are observed which can be assigned to Mo^{5+} from sub-stoichiometric oxide (MoO_x). The MoO_x is in turn believed to be originated from the reaction between molybdenum and oxygen after irradiation[74]. As to the region for S 2p, in addition to the signals correlated with MoS_2, the peaks with binding energy at 163.1 and 164.3 eV are identified, which are assumed to be part of free sulfur attached on the surface. The loss of sulfur is confirmed by the calculated Mo:S ratio of 1:2.3 with less sulfur compared to the unirradiated sample. With the dose increasing to 5000 μC/cm^2, the Mo:S ratio is further reduced to 1:2.25, indicating more vacancies introduced to the film. Meanwhile, we observed higher quantity of MoO_x and free sulfur as shown in Fig. 4e, f. The existence of MoO_x and free sulfur can be explained by the breaking of Mo-S bonds during e-beam irradiation process. The Mo with no S bonding to it would

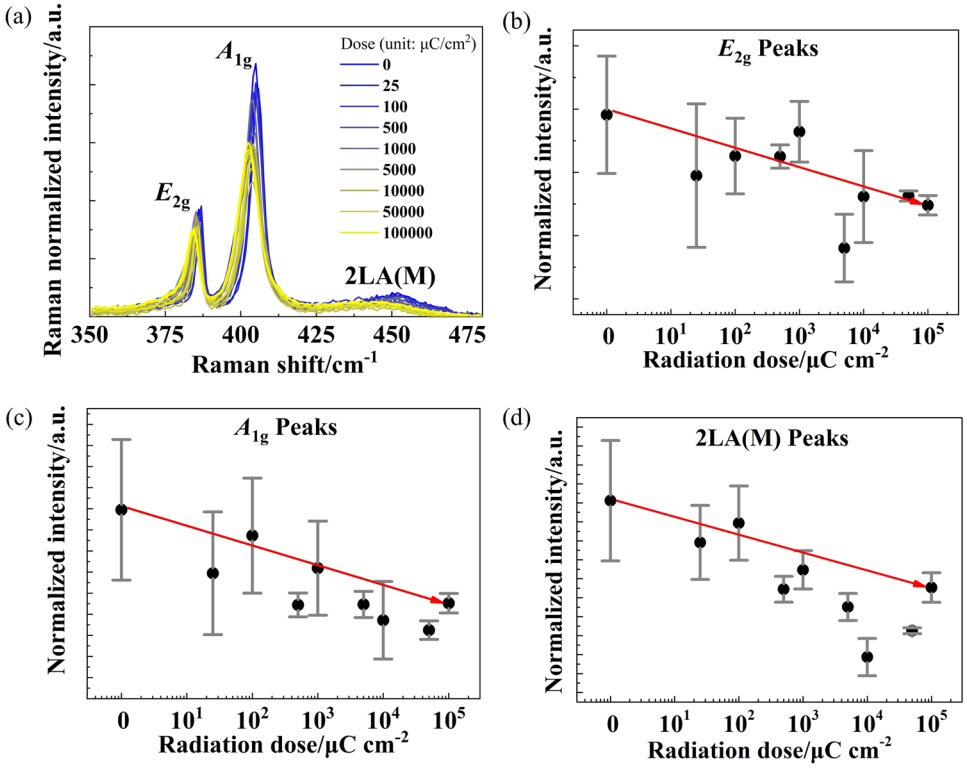

Fig. 3 Raman spectra analysis of the irradiation effect on monolayer MoS_2. a The Raman spectra of monolayer MoS_2 with different radiation doses up to 10^5 μC/cm^2. The peaks for unirradiated sample at ~386 cm^{-1} (E_{2g}) and 405 cm^{-1} (A_{1g}) are consistent with previous reports for monolayer MoS_2. **b** E_{2g} peak intensity, (**c**) A_{1g} peak intensity, and (**d**) 2LA(M) peak intensity with different radiation doses. A decrease of intensity can be observed as dose increases. The 2LA(M) peak disappears at high radiation doses. These suggest sulfur vacancies are introduced to the MoS_2 film after irradiation. The Raman spectra are measured on three different locations for each dose to compensate for variation from material growth.

combine with the oxygen to form sub-stoichiometric MoO_x due to a long-time exposure to air, while the S atoms become free sulfur and are attached to the surface. An appropriate cleaning process after irradiation may remove the free sulfur, but it was intentionally skipped to avoid possible influence due to the monolayer nature of the sample and accurately characterize the effect of the irradiation process on MoS_2 film. For the NVRS device fabrication in this work, top electrodes (TE) are deposited immediately after the irradiation step, considerably prevent the exposure to air and the formation of MoO_x, and the cleaning process is applied to remove any possible residues and by-products. Thus, based on the XPS analysis, sulfur vacancies are introduced to the MoS_2 film by the irradiation treatment. The regions of Mo 3d and S 2p for unirradiated, dose of 250 μC/cm^2, and dose of 5000 μC/cm^2 samples are compared together to show the irradiation effect on the MoS_2 film (see Supplementary Fig. 6). The loss of sulfur through electron irradiation process is confirmed by the extracted Mo:S ratio using a previously reported method, showing a ~3% reduction of sulfur for the sample with 250 μC/cm^2 dose and a ~5% reduction of sulfur for the sample with 5000 μC/cm^2 dose compared to unirradiated sample[75].

"Virtual" conductive points

Although the Raman and PL analysis can only indicate the creation of sulfur vacancies, it has been widely reported by other researchers that e-beam irradiation process can produce sulfur vacancies, which has been confirmed by various methods including direct observation using HR-TEM[61,69,76]. With the material analysis, we have confirmed that increasing irradiation dose would create more sulfur vacancies on the monolayer MoS_2 film. Post-irradiation process (TE-related patterning and deposition) may have certain effect on the surface property. However, referring to other reports with similar process[77–79] and our previous "transferred TE" devices (no TE patterning and deposition involved) that show similar NVRS phenomenon[49], the sulfur vacancies likely persist and play an important role in switching behavior in the MIM devices. The illustration of the irradiation effect is shown in Fig. 5. Our material characterizations strongly support that the high-energy electrons can break the bonds between Mo and S atoms in MoS_2 and remove sulfur from the lattice. With the subsequent cleaning and the immediate TE deposition after irradiation in the device fabrication process, sulfur vacancies are introduced to the monolayer MoS_2 film, which would impact the device performance. Based on our previous studies, conductive points —similar to conductive filaments in metal-oxide devices, can be formed through these induced vacancies and result in the resistive switching phenomenon in 2D-based devices[49,50]. A key difference is that the conductive point is 'virtual', i.e., not a physical connection that bridges the van der Waals gap and directly connects the top electrode to the bottom electrode, unlike conductive filaments which are direct physical connections. Benefiting from the ultrathin layer thickness, the resistance can have a noticeable change with only one side of vacancy filled by metal through the virtual conductive points. The existence of multiple conductive points further amplifies the resistance ratio between HRS and LRS. The comparison between "real" conductive filaments and "virtual" conductive points is presented in the supporting information as Supplementary Fig. 7. The virtual conductive point model is supported by our STM studies showing direct observation of the substitution of gold atoms into the sulfur vacancies, which leads to the HRS to LRS switching, indicating the essential role of sulfur vacancies in NVRS phenomenon[49,50]. In these studies, a combination of STM and

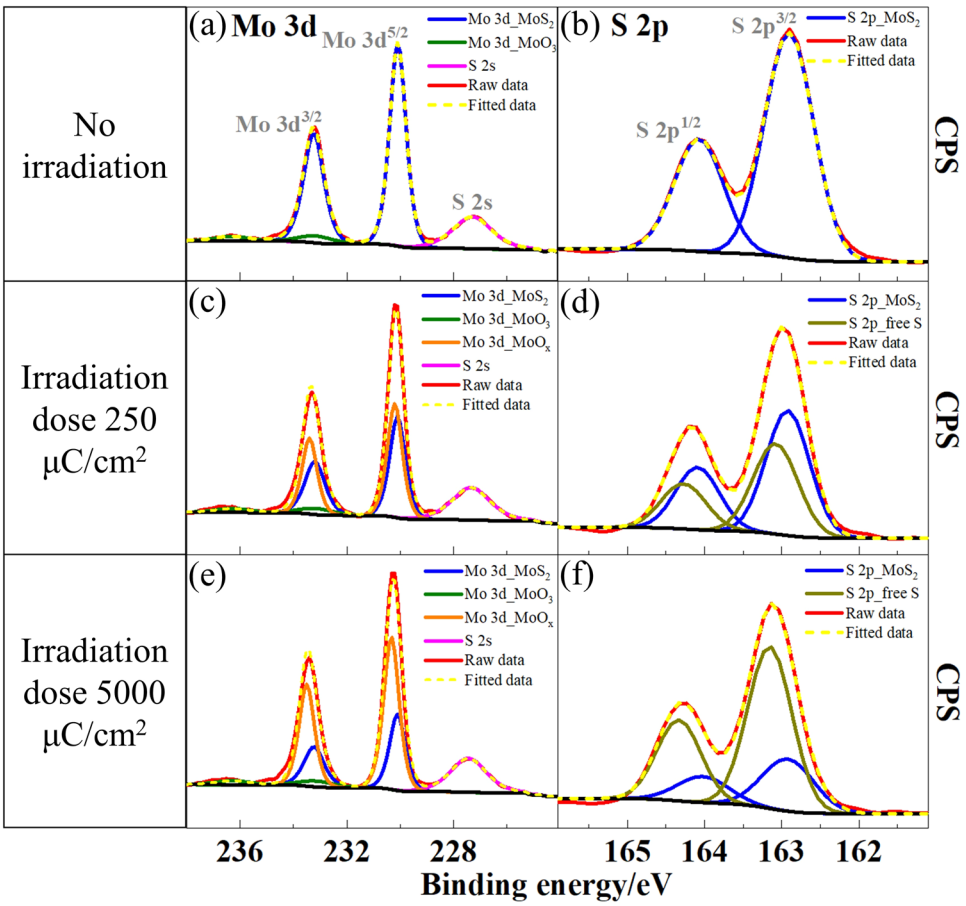

Fig. 4 XPS analysis of the irradiation effect on monolayer MoS_2. The XPS results of unirradiated sample in the regions of (**a**) Mo 3d and (**b**) S 2p, respectively. The presence of monolayer MoS_2 is confirmed by the characteristic peaks at 230.1 eV (Mo $3d^{5/2}$), 233.2 eV (Mo $3d^{3/2}$), 227.2 eV (S 2 s), 162.9 eV (S $2p^{1/2}$) and 164.1 eV (S $2p^{3/2}$). Small peaks at 233.1 eV and 236.32 eV indicate the presence of MoO_3 due to the exposure to air. **c**, d The XPS results of the sample after irradiation at the dose of 250 μC/cm^2. In addition to MoS_2 and MoO_3 that have been identified, sub-stoichiometric MoO_x and free sulfur are observed for the irradiated sample, which suggests the breaking of Mo-S bonds and the creation of sulfur vacancies. **e**, **f** The XPS results of the sample after irradiation at the dose of 5000 μC/cm^2. Lower peaks from MoS_2 and higher peaks from MoO_x and free sulfur are observed. Based on the extracted Mo:S ratio, compared to unirradiated sample, the sample with 250 μC/cm^2 dose shows a ~3% reduction of sulfur, and the sample with 5000 μC/cm^2 dose shows a ~5% reduction of sulfur, indicating a loss of sulfur as irradiation dose increases. The right *y*-axis refers to count per second (CPS).

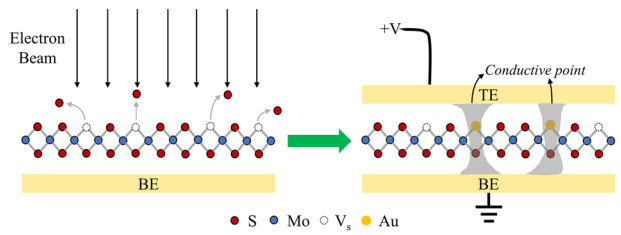

Fig. 5 Illustration of irradiation effect on MoS_2 film. High-energy electron beam breaks Mo-S bonds, leading to the creation of sulfur vacancies during the irradiation process. In the fabricated 2D memristors, these sulfur vacancies, with the metal atoms/ions from electrodes migrating into them, promote the formation of one or more virtual conductive point(s), which is responsible for the resistive switching phenomenon.

local transport studies is performed on 2D MoS_2 film on gold surfaces. The STM images recorded the initial state of the sulfur vacancy before voltage is applied on the tip and the state after RESET (corresponds to the HRS), and the state of the sulfur vacancy is substituted by a gold atom after SET (corresponds to the LRS). These images and the I–V curves between the states provide direct evidence in experiments to prove the virtual conductive point mechanism that the resistive switching phenomenon can be attributed to a single metal atom migration from electrodes to vacancy.

Representative non-volatile resistive switching behavior

Representative bipolar non-volatile resistive switching I–V curves of the MoS_2 devices are shown in Fig. 6. For an unirradiated device as an example (Fig. 6a), it is initially at a high-resistance state (HRS) at pristine state. By applying a positive voltage sweeping, the current suddenly increases at ~1.25 V, indicating a transition from a HRS to a low-resistance state (LRS), which is commonly referred to as a "SET" process. To RESET the device, a negative voltage sweeping is applied in a bipolar operation, where the current decreases at ~−0.48 V, indicating a transition from LRS back to HRS. A compliance current is applied during the SET process to prevent the device from irreversible breakdown due to unconstrained high current, while for RESET process the compliance current is not needed. After SET or RESET, the device can remain at LRS or HRS without external power supply, demonstrating the non-volatility of the switching behavior. Electro-forming process, a prerequisite that commonly exists in bulk oxide-based devices to initialize a soft dielectric breakdown for filament formation, is not required for 2D-based atomristors, which is expected to reduce

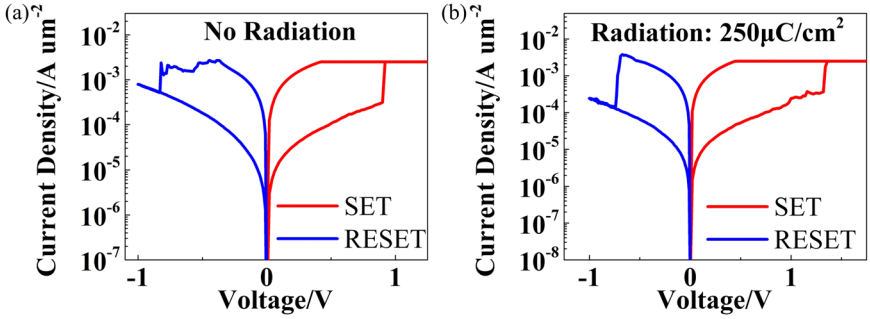

Fig. 6 Representative I–V switching curves of MoS_2-based NVRS devices. Typical bipolar I–V curves (*y*-axis in current density) of resistive switching behavior in (**a**) unirradiated devices and (**b**) devices with e-beam irradiation treatment at dose of 250 μC/cm^2.

the power consumption in practical applications[25]. With MoS_2 film irradiated by electron-beam, the devices exhibit similar resistive switching characteristics in the I–V curves. Figure 6b shows a representative switching curve for a MoS_2 device under 250 μC/cm^2 irradiation dose, with a SET voltage at ~1.32 V and a RESET voltage at ~−0.68 V. More switching curves for devices with irradiation dose ranging from 10 to 10,000 μC/cm^2 are included in Supplementary Fig. 8 in supporting information. Higher doses up to 10^6 μC/cm^2 have also been applied on the MoS_2 films. However, those devices cannot show resistive switching behavior, possibly due to the excessive amount of induced sulfur vacancies which lead to an electrical short of the device. Current levels at LRS and HRS are commonly used as the key metrics in the study of memristors to obtain the ON/OFF current ratio and estimate the power consumption[21,25]. However, considering the interest of current density from a wider range of researchers, we use current density (current normalized to the lateral area of the device) in the I–V curves shown in Fig. 6 and Supplementary Fig. 8. The typical ON-state current density is calculated to be ~2.5×10^5 A/cm^2 (or 2.5×10^{-3} A/μm^2), which is within the reasonable range compared with both other emerging 2D-based devices and traditional bulk oxide-based devices[40,80,81]. The relatively high current level/current density has been widely recognized and studied for memristors[25]. For the MoS_2-based devices, the high current density can partly be originated from the extremely thin active layer thickness. This can be explained by reviewing the formula of current density: $J = \sigma^* E$, where J is current density, σ is conductivity, and E is electric field. The electric field E is further determined by voltage and distance between two electrodes ($E = V/d$). With the same external bias, monolayer MoS_2 is only ~0.7 nm in thickness, which results in a larger electric field and thus a higher current density. Another factor that may attribute to the ON-state current is the property of the virtual conductive points, which determines the conductivity σ. According to our previous studies on the temperature-dependent conduction current[47], the LRS shows an *Ohmic-like metallic conduction* behavior, which is consistent with our proposed model that electrons transport through the adsorbed metal atoms at the defect locations. Moreover, comparing to single conductive filament in bulk materials-based devices, the current density is expected to be larger with multiple conductive paths formed in MoS_2-based devices. Note that although the current density of memristors can be quite high, it is still far less than that of typical metals under the same conditions. The current density of a typical metal - copper, if placed at active layer in our NVRS device, is calculated to be $J = \sigma^* E = \sigma^*(V/d) = 4.26 \times 10^{12}$ A/cm^2, where V is determined by the voltage where highest current typically happens at 0.5 V and the conductivity of copper at 20 °C is 5.96×10^7 S/m[82]. This is much higher than our calculated ON-state current density for MoS_2 devices at ~2.5×10^5 A/cm^2. At LRS, the high current flowing through the active layer produces *Joule heating* that is believed to drive metal atoms/ions out of the vacancies and result in the RESET process. On the other hand, the high current stress may also contribute to cycling failure of the device, which requires future studies to elucidate.

Statistical analysis on the reliability

Similar to the bulk metal-oxide RRAM in the early stages, the reliability of 2D-based memristors was not optimized[22,25]. For example, the monolayer MoS_2-based devices only had ~10% yield at the beginning. Although it subsequently increases to ~50% with the improved fabrication techniques, the yield is still relatively low for modern semiconductor industry integration. Moreover, as to the endurance, most of the devices can barely survive 20 DC cycles, with the highest cycle number at around 150. Although the retention time does not match the 10-year retention of the bulk oxide devices (>4 weeks in our previous report)[46], it has already outperformed other emerging 2D NVRS devices[35,40,42,45]. Thus, in this work, we focus on yield and endurance that limit the monolayer-based devices. The reliability issues, not only found in the emerging 2D-based NVRS devices but also in well-studied metal-oxide devices, are believed to originate from the stochastic nature of the resistive switching behavior[83,84]. Defects commonly exist in the 2D thin films (e.g. sulfur vacancies in MoS_2 film) and can play an important role in the electrical characteristics[77,85]. Our recent STM study has demonstrated the metal ion substitution into the sulfur vacancy can produce the resistive switching phenomenon in monolayer MoS_2[50]. Further investigations using current-sweep and constant electric stress method show multiple resistance states during switching, which is assumed to be related with multiple defect-rich regions on the 2D layers[86,87]. Thus, it is essential to explore an approach to precisely control the surface properties with advanced defect engineering techniques for better performance of the 2D memristors. Electron-beam irradiation has been used to produce defects in MoS_2 films[59–61]. With the material characterizations by Raman and PL spectra and XPS, we observed higher amount of sulfur vacancies by applying e-beam irradiation. Statistical electrical measurements were performed on the atomristor devices to evaluate the reliability. For each irradiation dose, ~15 devices have been tested to acquire the statistical results on endurance, and more detailed numbers are included in the supporting information as Table S1. In traditional metal oxide RRAM, yield is mostly related with forming failures[88,89]. Owning to the forming-free characteristic of our atomristor[47], we define yield as the ratio of atomristor devices that work properly (can be operated through at least a complete SET and RESET cycle) to the total number of devices measured. For successful SET/RESET process, it is referred to resistive switching process switch the device resistance state with the On/Off ratio > 3[90]. Figure 7a shows the number of DC cycles that the MoS_2-based memristors can operate with different irradiation doses. The first data point refers to the devices with no irradiation, showing an average of only ~6 cycles. With increasing dose applied to the MoS_2 film, the DC endurance performance

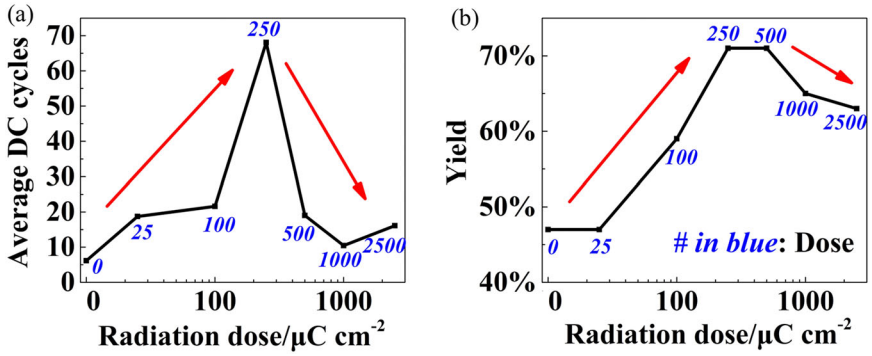

Fig. 7 The irradiation effect on the reliability performance of MoS_2 devices. a The average DC cycle number for the devices with different radiation doses. The average DC cycles that one device can survive increase from ~6 cycles for unirradiated devices to ~68 cycles as the dose increases to 250 μC/cm^2, and then return back to a lower level at higher doses. **b** The yield for the devices with different radiation doses. The yield increases from ~47% for unirradiated device to ~71% as the dose increases to 250 μC/cm^2 and 500 μC/cm^2, and then returns back to a lower level at higher doses.

increases to an average of ~68 cycles (with a peak of 240 cycles) for devices irradiated at 250 μC/cm^2, indicating a > 11x improvement compared to the unirradiated devices. This can be attributed to the introduced sulfur vacancies enabling more conductive points during switching. After each resistive switching cycle, there is a possibility for a conductive point to temporarily not work for the next cycle. According to our proposed mechanism, the resistive switching depends on the dissociation, diffusion, and adsorption of metal atom/ion from electrodes that substitutes into the sulfur vacancy[49]. These processes may be affected by a number of factors such as interface properties or bias conditions, which causes the conductive point to not work in certain cycle, similar to the failure of conductive filament in metal-oxide devices[25,91]. Compared with unirradiated devices, the devices with higher radiation dose have more redundant conductive points so that they have a less possibility for all the conductive points to fail. Thus, the irradiated devices can operate for more cycles before failing. However, as the doses continue to increase, the endurance performance falls back to an average of ~20 DC cycles. A possible reason is that the higher doses will induce excessive amount of sulfur vacancies that lead to a large current, which causes an irreversible breakdown for the device. Note that the cycling failure happens with a high current despite the irradiation dose. Devices with higher dose have a higher possibility to have excessive conductive points that lead to device failure due to Joule heating. The peak cycling number at 250 μC/cm^2 suggests an irradiation treatment with a moderate dose is desirable for the 2D memristors to operate for a longer time.

Yield is another concern in MoS_2-based NVRS devices that limits the potential applications. Figure 7b shows the yield of the fabricated devices with different irradiation doses. For each dose, we have tested ~15 devices to get the statistical results. The yield for unirradiated devices is 47%, which is consistent with our expectation for pristine monolayer MoS_2 memristors. With the application of e-beam irradiation, the yield gradually increases to 71% for the devices at 250 μC/cm^2 and 500 μC/cm^2. The increasing yield can be explained by the increasing amount of sulfur vacancies that promote more conductive points formation in the resistive switching. With increasing S vacancies, there is less possibility that a device has no conductive point formed, this in turn increasing the overall yield. Similar to the case of DC cycles, as the irradiation dose further increases, the yield would decrease to a relatively low level at 63%. This phenomenon can be attributed to the large number of vacancies in the films, which results in a high possibility of cluster formation that makes some of the devices fail. The profile of yield and average DC cycle number under different irradiation doses has been included in the supporting information as Table S1.

Monte Carlo simulations on electron irradiation effect

Based on these reliability test results, it has been found that the optimum performance can be achieved with a moderate irradiation dose (at ~250 μC/cm^2 for monolayer MoS_2-based memristors). A weak e-beam irradiation treatment cannot provide sufficient vacancies for a stable switching phenomenon, while excessive irradiation treatment would introduce overwhelming vacancies that lead to a cluster of defects or a high conduction current, which causes an irreversible breakdown. To support our hypothesis, we performed simulation works using Monte Carlo method to illustrate the effect of the induced vacancies on the electrical performance of the devices. Owing to the stochastic nature of resistive switching phenomenon, Monte Carlo method has been used as one of the most suitable tools to mimic the random process for NVRS devices[92,93]. First, we studied the electron irradiation effect on device yield. We have learned that more sulfur vacancies exist in monolayer MoS_2 as radiation dose increases. As a result, the possibility of forming conductive points will be higher, which is beneficial to obtain a higher yield. According to our previous STM measurements on single sulfur vacancy, resistive switching phenomenon can be observed in 5–10% of all tested vacancies. In our simulation, we assume a certain percentage of vacancies can work as a conductive point to produce the resistive switching behavior. As long as the device has at least one vacancy serving as conductive point, it is deemed as a working device. The rate of conduction with the consideration of conductive point formation (R_{cp}) can be theoretically expressed as (Eq. (1)):

$$R_{cp} = 1 - (1 - P)^n \quad (1)$$

where $P = 0.05$ is the possibility of a sulfur vacancy working as a conductive point, and n is the number of vacancies. The simulated R_{cp} (Supplementary Fig. 9a) is consistent with Eq. (1). It can be seen that R_{cp}, which can also be referred to as the ratio of the working devices to all devices, increases with higher amount of vacancies. With more switchable vacancy cites, there is less chance for irreversible hard breakdown during the SET process due to lack of available sulfur vacancies. Nevertheless, as vacancy number increases, the possibility of forming clusters (multiple vacancies closely located) also increases, which is another factor that must be taken into consideration. This cluster effect would lead to significant metal diffusion in this region and result in a direct conduction between electrodes. A supporting evidence for this assumption is that most failed devices with high irradiation dose are tested to be short-circuit in experiments, possibly due to the direct conduction through the cluster of vacancies. Monte Carlo simulations were performed to visualize the cluster effect. Figure 8a shows a typical top-view distribution of 15 sulfur

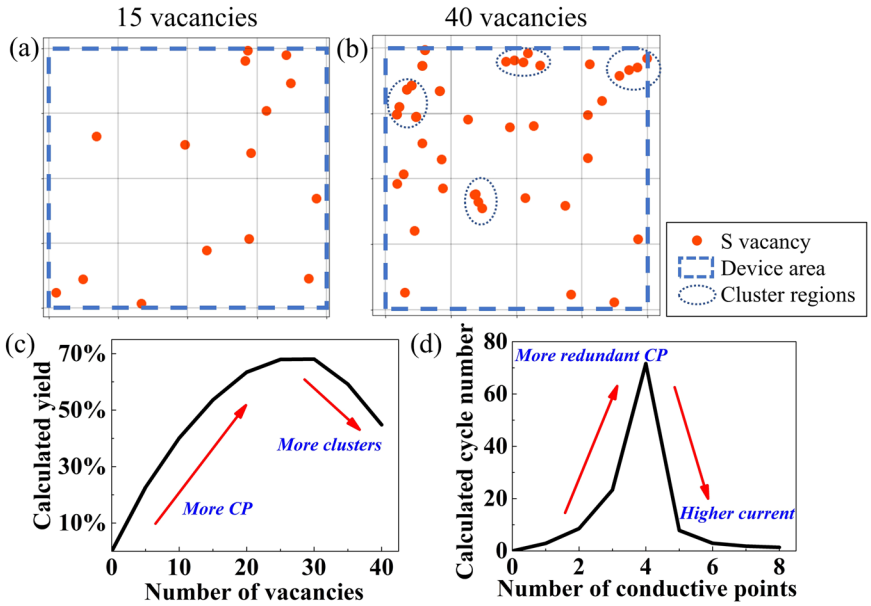

Fig. 8 Monte Carlo simulations to illustrate the irradiation effect on reliability. Representative distribution of sulfur vacancy within the device area with (**a**) 15 vacancies and (**b**) 40 vacancies shown in top view. The vacancies are randomly located in the device area. More vacancies will lead to a higher possibility of clusters formation in the film, which is assumed to reduce the yield due to severe leakage through these clusters that short the electrodes through the MoS_2. **c** The calculated yield using Monte Carlo simulation to illustrate two mechanisms that affects device yield: at low radiation dose, yield increases as vacancy number increases due to more (virtual) conductive points formed; at high radiation dose, yield decreases as vacancy number increases due to more clusters formed. **d** The calculated cycle number using Monte Carlo simulation to illustrate two mechanisms that affect device endurance: at low radiation dose, cycle number increases as conductive point number increases due to more redundant conductive points available; at high radiation dose, cycle number decreases as conductive point number increases due to excessive Joule heating induced by high current.

vacancies randomly placed in the device area. No obvious cluster can be seen in the image where most vacancies are far from each other. If the number of vacancies is increased to 40, a few cluster regions will be observed as noted in Fig. 8b. A clear trend of generation of vacancy clusters with excessive vacancies is suggested by this qualitative Monte Carlo simulations. Though specific vacancy number does not necessarily correspond to real defect density, qualitative Monte Carlo simulations enable deeper understanding of potential effects of vacancies number on reliability of devices. For simplicity of statistics, the device area is equally divided into a 4×4 grid, and the presence of cluster is defined to be the scenario that at least 5 vacancies are located in the same 1×1 cell. The rate of cluster (R_{cl}), as a parameter to characterize failed devices, is included in Supplementary Fig. 9b, showing an increasing possibility of clusters formation in MoS_2 as vacancy number increases. The overall yield (Y) can thus be expressed by [Eq. 2]:

$$Y = R_{cp} \cdot (1 - R_{cl}) = (1 - (1 - P)^n) \cdot (1 - R_{cl}) \quad (2)$$

which is shown in Fig. 8c based on the simulation results with the two opposite effects (conductive points and clusters) in the model together. To have a confidence interval of over 95%, 1000 times of iteration were made for each number of vacancies. Compared with the experimental results in Fig. 7b, the simulated yield exhibits similar trend that the yield first increases and then decreases, indicating the conductive points effect dominates at low radiation dose (less vacancies), while the opposite cluster effect dominates at high radiation dose (more vacancies).

In addition to yield, Monte Carlo simulations have also been performed to study the irradiation effect on endurance. With higher radiation dose, more sulfur vacancies are introduced to the film, leading to a higher possibility of more conductive points formed. Since the endurance characterization is for working devices, it is more straightforward to modify the number of conductive points instead of vacancies. To simulate the cycles that a device can operate, we assume that in each cycle, there is a possibility for one conductive point to be not working. If there is at least one conductive point working, the device enters next cycle for another evaluation. However, if all the conductive points are not working, the device is deemed a failed device and this cycle number is recorded as the endurance. An average cycle number is calculated by repeating this process for 1000 simulated devices. As the number of conductive points increases, the endurance is expected to be higher due to more redundant conductive points available that reduce the possibility of device failure at each cycle. On the other hand, with the increasing number of conductive points, there will be a higher chance for the device to get a large conduction current. According to the experimental observation, the cycling failure in MoS_2-based devices mostly happens with a large current at LRS so that the device cannot undergo the RESET process afterwards, which is consistent with our assumption. This phenomenon can be explained by the Joule heating induced by the high current. In normal switching, such Joule heating effect is desired to trigger the RESET process[25]. However, excessive heating will cause an irreversible breakdown of the device. To characterize the impact of the high current on cycling performance, the possibility of high current existence (at least 5 conductive points working in the same cycle) is included in Supplementary Fig. 9c. By taking both effects (redundant conductive points and high current) into consideration in the model, the simulated average cycle number is shown in Fig. 8d, exhibiting similar trend as compared to the experimental results (Fig. 7a). It can thus be inferred that redundant conductive point effect dominates at low radiation dose (less conductive points), while the opposite high current effect dominates at high radiation dose (more vacancies), leading to the phenomenon that the peak cycle number happens at a moderate radiation dose. These Monte Carlo simulations help illustrating the underlying physics of the electron irradiation effect that connects the material property with the electrical

performance and provide evidence to support the conductive-point model for resistive switching behavior in MoS_2-based NVRS devices. These results inspire further theoretical works with more advanced simulation approaches to develop a comprehensive model for the irradiation effect.

DISCUSSIONS

Other switching characteristics have been studied through statistical measurements, including DC cycling variability (Supplementary Fig. 10), SET/RESET voltage (Supplementary Fig. 11), ON/OFF resistance (Supplementary Fig. 12), and RESET current (Supplementary Fig. 13) with different irradiation doses. No clear trends were detected as function of irradiation doses, with a total of 67 working devices for 1575 DC measured cycles. This vacancy number independence can be related to the localized nature of virtual conductive-point[49,50], which has been observed for conductive filaments[94–96]. However, due to the stochastic nature of the switching phenomenon as discussed above, it is also possible that the difference of these switching parameters can be hidden behind the device-to-device and cycle-to-cycle variation. Currently, the stochastic nature of conductive-point/filament remains challenging to memristor research and commercialization, which requires more future efforts for optimization.

The endurance of 2D MoS_2 memristors in this work is typically tested/operated with DC voltage sweep(SET/RESET), which has been extended employed in our previous studies and is relatively well understood[46–50]. Besides the material/defect engineering, endurance can also be improved with moderate program/erase operation. In general, pulse tests would induce less electric stress compared to DC cycling, and thus can produce higher endurance. In Graphene oxide-based memristor, a higher number of switching cycles (~450 cycles) was achieved and reported with pulse bias, than 120 cycles with DC bias[97]. Endurance can be further improved with optimized pulse test conditions[98]. More than 10^6 switching cycles were obtained on HfO_2-based RRAM with reported new pulse operation method, while the endurance with the traditional pulse method was less than 10^3 cycles. Optimizing the pulse cycling test condition for endurance enhancement is out of the scope of this work. However, for practical applications, it is an important matter that will be the focus of future studies.

The monolayer-based memristors, at an early development stage, is not yet competitive compared with the well-studied metal-oxide memristors. However, the 2D monolayers offer extreme vertical scalability (high speed and low power consumption owing to thinner active layer thickness) and better flexibility (potential applications in wearable electronics). In addition, the monolayer MoS_2 memristors have already shown comparable or even better switching speed, ON/OFF ratio, switching voltage, and the forming-free characteristics (forming process is mostly required in oxide-based memristors). Taking advantage of the low ON resistance, we have proposed and realized a new application of RF switch based on monolayer memristor, which exhibits the record performance over all other emerging switches[99,100]. With the defect engineering methodology that has been discussed in this work, and the advances in 2D material growth, mechanism understanding, device structure & process flow optimization, testing technology, etc., it is expected that the vacancy property can be precisely controlled to achieve a better performance for the 2D NVRS devices. Table S2 shows the comparison among representative emerging 2D material-based memristors, where our monolayer-based devices have exhibited superior performance over others.

In summary, we report an effective method by electron irradiation to investigate the defect properties on monolayer MoS_2, which considerably improves the reliability of the 2D-based memory devices. Material characterizations, including Raman, PL and XPS measurements, have been performed on the irradiated film and clearly show that sulfur vacancies are introduced through the irradiation process. The statistical electrical studies results suggest a moderate radiation dose is desired to achieve the highest yield and DC cycling endurance. Monte Carlo simulations have been conducted to elucidate the relationship between the induced sulfur vacancies and the enhanced reliability. The irradiation effect on device characteristics can be explained by the virtual conductive-point model that the resistive switching behavior is attributed to the metal ion migration into the sulfur vacancy. Monte Carlo simulations further illustrate the physical process behind the irradiation effect and reveal device failure mechanisms of clustering or excessive Joule heating. The results reported here provide additional insights into defect engineering for improving the performance, yield and reliability of 2D NVRS devices for various applications including flexible non-volatile memory, neuromorphic computing, and RF switches.

METHODS

Device fabrication

The monolayer CVD-grown MoS_2 films on SiO_2/Si substrate were purchased from Sixcarbon Technology. All the fabricated devices in this work are in crossbar MIM structure. The BE were patterned by e-beam lithography and deposited by e-beam evaporator (2 nm Cr/80 nm Au) on a 285 nm SiO_2/Si substrate. The monolayer MoS_2 film was then transferred on the target substrate with BE on it using polydimethylsiloxane (PDMS) stamp transfer method. In this method, the MoS_2 film is brought into conformal contact with PMDS stamp. Then, the substrate-MoS_2-PDMS system was soaked into deionized water for about 30 min. Since SiO_2 on the substrate is hydrophilic, it is easy for water to diffuse into the interface between MoS_2 and SiO_2. The MoS_2-PDMS film was separated from SiO_2/Si substrate and brought into contact with the target substrate. The PDMS stamp was subsequently peeled off, leaving MoS_2 on the target substrate. After transferring, TE were patterned and deposited using the same methods as BE. The device area is defined as the overlapped region between TE and BE, which is $2 \times 2\ \mu m^2$ in this work. Electron-beam irradiation was performed using a Raith eLINE electron beam lithography system with Raith NanoSuite software to control the exposing dose and area. The electron beam voltage is 20 kV, and the beam current is ~5 nA with 120 um aperture on different locations.

Material and electrical characterization

Raman spectroscopy and PL were performed to evaluate the MoS_2 film before and after transferring on a Renishaw in-Via system using a 532 nm wavelength source. The material characterizations before transferring are only used to confirm the quality of the purchased 2D films (not shown in this paper). The Raman and PL data presented in this paper (including the unirradiated and irradiated samples) are all collected after transferring. XPS spectra were recorded using a commercial X-ray photoelectron spectrometer (Kratos Axis Ultra DLD, Manchester, U.K.), utilizing a monochromated Al-Ka X-ray source ($h_v = 1486.5$ eV), hybrid optics (employing a magnetic and electrostatic lens simultaneously) and a multi-channel plate coupled to a hemispherical photoelectron kinetic analyzer. The spectrometer was calibrated using the Cu $2p^{3/2}$, Ag $3d^{5/3}$, and Au $4f^{7/2}$ peaks. Samples were stored and transported to the XPS lab in a vial under ambient air. Spectra were collected with two separate pass energies of 20 and 40 eV at 0.1 eV per step, and 4 sweeps. Areas of analysis on the sample were collected using the aperture of a circular area with a 110 um diameter. Since samples were charging during data acquisition, the charge neutralizer was turned on, shifting all peaks to lower binding energies by 2.0–2.5 eV. Consequently, the binding energy of the peaks were calibrated with respect to the adventitious hydrocarbon C 1 s at 284.8 eV. Casa XPS analysis software was used for peak analysis and the stoichiometry of samples was determined using the Kratos' library for the relative sensitivity factors of the elements of interest. The DC characteristics of the devices were taken on a Cascade probe station with an Agilent 4156 semiconductor parameter analyzer under ambient conditions.

Monte Carlo simulation

For simulations of yield corresponding with the distribution of vacancies, we used a 2D Monte Carlo model. Vacancies are distributed in a 4*4 grid. In this model, several assumptions are made: (1) The abscissa and

ordinate of each vacancy follow uniform distribution. (2) Each vacancy has the same probability to become a virtual conductive point. Here, we use 5% as the rate of being conductive to be consistent with previous STM results. (3) When there are at least 5 vacancies in a 1*1 area within the simulated area, it will be defined as a cluster. In this simulation, the number of vacancies varies from 5 to 40. To have a confidence interval of over 95%, 1000 times of iteration were made for each number of vacancies. The device with at least one conductive point and without cluster formed is defined as a working device. The yield is calculated to be the portion of working devices in all the 1000 simulated devices for each dose.

For Monte Carlo simulations of endurance (cycle number) correlated with conductive points, we assumed that, at each cycle, each conductive point has the same possibility (35%) to be not working in this cycle. In this simulation, the number of conductive points varies from 1 to 8. Similarly, to have a confidence interval of over 95%, 1000 times of iteration were made for each number of conductive points. If in one cycle, the device has no conductive point working, or has at least 5 conductive points working (a high-current state), the device is defined as failed and the cycle number is recorded as the endurance for this device. Otherwise, the device enters next cycle for another evaluation, until the device fails at certain cycle. The overall endurance for each number of conductive points is the average of cycle number for all the 1000 simulated devices.

DATA AVAILABILITY

The data that support the plots within this paper and other finding of this study are available from corresponding author upon reasonable request.

CODE AVAILABILITY

Upon request, authors will make available any previously unreported computer code or algorithm used to generate results that are reported in the paper and central to its main claims.

Received: 29 September 2021; Accepted: 31 March 2022;
Published online: 09 May 2022

REFERENCES

1. Bhimanapati, G. R. et al. Recent Advances in Two-Dimensional Materials beyond Graphene. *ACS Nano* **9**, 11509–11539 (2015).
2. Akinwande, D. et al. A review on mechanics and mechanical properties of 2D materials-Graphene and beyond. *Extrem. Mech. Lett.* **13**, 42–77 (2017).
3. Choi, W. et al. Recent development of two-dimensional transition metal dichalcogenides and their applications. *Mater. Today* **20**, 116–130 (2017).
4. Akinwande, D., Petrone, N. & Hone, J. Two-dimensional flexible nanoelectronics. *Nat. Commun.* **5**, 12 (2014).
5. Novoselov, K. S. et al. Electric field effect in atomically thin carbon films. *Science* **306**, 666–669 (2004).
6. Radisavljevic, B., Radenovic, A., Brivio, J., Giacometti, V. & Kis, A. Single-layer MoS2 transistors. *Nat. Nanotechnol.* **6**, 147–150 (2011).
7. Akinwande, D. et al. Graphene and two-dimensional materials for silicon technology. *Nature* **573**, 507–518 (2019).
8. Illarionov, Y. Y. et al. Insulators for 2D nanoelectronics: the gap to bridge. *Nat. Commun.* **11**, 15 (2020).
9. Tao, L. et al. Silicene field-effect transistors operating at room temperature. *Nat. Nanotechnol.* **10**, 227–231 (2015).
10. Park, J. H. et al. Large-Area Monolayer Hexagonal Boron Nitride on Pt Foil. *ACS Nano* **8**, 8520–8528 (2014).
11. Ling, X., Wang, H., Huang, S. X., Xia, F. N. & Dresselhaus, M. S. The renaissance of black phosphorus. *Proc. Natl Acad. Sci. USA* **112**, 4523–4530 (2015).
12. Wang, Q. H., Kalantar-Zadeh, K., Kis, A., Coleman, J. N. & Strano, M. S. Electronics and optoelectronics of two-dimensional transition metal dichalcogenides. *Nat. Nanotechnol.* **7**, 699–712 (2012).
13. Castro Neto, A. H., Guinea, F., Peres, N. M. R., Novoselov, K. S. & Geim, A. K. The electronic properties of graphene. *Rev. Mod. Phys.* **81**, 109–162 (2009).
14. Jariwala, D., Sangwan, V. K., Lauhon, L. J., Marks, T. J. & Hersam, M. C. Emerging Device Applications for Semiconducting Two-Dimensional Transition Metal Dichalcogenides. *ACS Nano* **8**, 1102–1120 (2014).
15. Mak, K. F., Lee, C., Hone, J., Shan, J. & Heinz, T. F. Atomically Thin MoS2: a new direct-gap semiconductor. *Phys. Rev. Lett.* **105**, 4 (2010).
16. Cassabois, G., Valvin, P. & Gil, B. Hexagonal boron nitride is an indirect bandgap semiconductor. *Nat. Photon.* **10**, 262-+ (2016).
17. Ismach, A. et al. Toward the Controlled Synthesis of Hexagonal Boron Nitride Films. *ACS Nano* **6**, 6378–6385 (2012).
18. Mounet, N. et al. Two-dimensional materials from high-throughput computational exfoliation of experimentally known compounds. *Nat. Nanotechnol.* **13**, 246-+ (2018).
19. Chen, A. A review of emerging non-volatile memory (NVM) technologies and applications. *Solid-State Electron* **125**, 25–38 (2016).
20. Wong, H. S. P. & Salahuddin, S. Memory leads the way to better computing. *Nat. Nanotechnol.* **10**, 191–194 (2015).
21. Lanza, M. et al. Recommended Methods to Study Resistive Switching Devices. *Adv. Electron. Mater.* **5**, 28 (2019).
22. Jeong, D. S. et al. Emerging memories: resistive switching mechanisms and current status. *Rep. Prog. Phys.* **75**, 31 (2012).
23. Zahoor, F., Zulkifli, T. Z. A. & Khanday, F. A. Resistive Random Access Memory (RRAM): an Overview of Materials, Switching Mechanism, Performance, Multilevel Cell (mlc) Storage, Modeling, and Applications. *Nanoscale Res. Lett.* **15**, 26 (2020).
24. Ielmini, D. Resistive switching memories based on metal oxides: mechanisms, reliability and scaling. *Semicond. Sci. Technol.* **31**, 25 (2016).
25. Wong, H. S. P. et al. Metal-Oxide RRAM. *Proc. IEEE* **100**, 1951–1970 (2012).
26. Chen, Y. C. et al. A Novel Resistive Switching Identification Method through Relaxation Characteristics for Sneak-path-constrained Selectorless RRAM application. *Sci. Rep.* **9**, 6 (2019).
27. Zhou, F., Chang, Y. F., Byun, K., Fowler, B. & Lee, J. C. Characterization of external resistance effect and performance optimization in unipolar-type SiOx-based resistive switching memory. *Appl. Phys. Lett.* **105**, 4 (2014).
28. Wang, C. Y. et al. 2D layered materials for memristive and neuromorphic applications. *Adv. Electron. Mater.* **6**, 1901107 (2020).
29. Tan, C. L., Liu, Z. D., Huang, W. & Zhang, H. Non-volatile resistive memory devices based on solution-processed ultrathin two-dimensional nanomaterials. *Chem. Soc. Rev.* **44**, 2615–2628 (2015).
30. Hui, F. et al. Graphene and Related Materials for Resistive Random Access Memories. *Adv. Electron. Mater.* **3**, 32 (2017).
31. Pradhan, S. K., Xiao, B., Mishra, S., Killam, A. & Pradhan, A. K. Resistive switching behavior of reduced graphene oxide memory cells for low power nonvolatile device application. *Sci. Rep.* **6**, 9 (2016).
32. Cheng, P. F., Sun, K. & Hu, Y. H. Memristive Behavior and Ideal Memristor of 1T Phase MoS2 Nanosheets. *Nano Lett.* **16**, 572–576 (2016).
33. Bessonov, A. A. et al. Layered memristive and memcapacitive switches for printable electronics. *Nat. Mater.* **14**, 199–204 (2015).
34. Son, D. et al. Colloidal Synthesis of Uniform-Sized Molybdenum Disulfide Nanosheets for Wafer-Scale Flexible Nonvolatile Memory. *Adv. Mater.* **28**, 9326-+ (2016).
35. Xu, R. J. et al. Vertical MoS2 Double-Layer Memristor with Electrochemical Metallization as an Atomic-Scale Synapse with Switching Thresholds Approaching 100 mV. *Nano Lett.* **19**, 2411–2417 (2019).
36. Zhang, F. et al. Electric-field induced structural transition in vertical MoTe2- and Mo1-xWxTe2-based resistive memories. *Nat. Mater.* **18**, 55-+ (2019).
37. Belete, M. et al. Nonvolatile Resistive Switching in Nanocrystalline Molybdenum Disulfide with Ion-Based Plasticity. *Adv. Electron. Mater.* **6**, 7 (2020).
38. Bhattacharjee, S. et al. Insights into Multilevel Resistive Switching in Monolayer MoS2. *ACS Appl. Mater. Interfac.* **12**, 6022–6029 (2020).
39. Wang, M. et al. Robust memristors based on layered two-dimensional materials. *Nat. Electron.* **1**, 130–136 (2018).
40. Pan, C. B. et al. Coexistence of Grain-Boundaries-Assisted Bipolar and Threshold Resistive Switching in Multilayer Hexagonal Boron Nitride. *Adv. Funct. Mater.* **27**, 10 (2017).
41. Chen, S. C. et al. Wafer-scale integration of two-dimensional materials in high-density memristive crossbar arrays for artificial neural networks. *Nat. Electron.* **3**, 638–645 (2020).
42. Hao, C. X. et al. Liquid-Exfoliated Black Phosphorous Nanosheet Thin Films for Flexible Resistive Random Access Memory Applications. *Adv. Funct. Mater.* **26**, 2016–2024 (2016).
43. Zhao, L. et al. Ultrathin (~ 2nm) HfOx as the fundamental resistive switching element: Thickness scaling limit, stack engineering and 3D integration. *2014 Ieee International Electron Devices Meeting (IEDM)*. 6.6. 1-6.6. 4 (2014).
44. Sangwan, V. K. et al. Gate-tunable memristive phenomena mediated by grain boundaries in single-layer MoS2. *Nat. Nanotechnol.* **10**, 403–406 (2015).
45. Sangwan, V. K. et al. Multi-terminal memtransistors from polycrystalline monolayer molybdenum disulfide. *Nature* **554**, 500-+ (2018).
46. Ge, R. et al. Atomristors: Memory Effect in Atomically-thin Sheets and Record RF Switches. *2018 Ieee International Electron Devices Meeting (IEDM)*. 22.26. 21-22.26. 24 (2018).
47. Ge, R. et al. Atomristor: nonvolatile resistance switching in atomic sheets of transition metal dichalcogenides. *Nano Lett.* **18**, 434–441 (2018).

48. Wu, X. H. et al. Thinnest Nonvolatile Memory Based on Monolayer h-BN. *Adv. Mater.* **31**, 7 (2019).
49. Ge, R. J. et al. A Library of Atomically Thin 2D Materials Featuring the Conductive-Point Resistive Switching Phenomenon. *Adv. Mater.* **33**, 9 (2021).
50. Hus, S. M. et al. Observation of single-defect memristor in an MoS2 atomic sheet. *Nat. Nanotechnol.* **16**, 58–62 (2021).
51. Mitra, S., Kabiraj, A. & Mahapatra, S. Theory of nonvolatile resistive switching in monolayer molybdenum disulfide with passive electrodes. *npj 2D Mater. Appl.* **5**, 11 (2021).
52. Wang, S., Robertson, A. & Warner, J. H. Atomic structure of defects and dopants in 2D layered transition metal dichalcogenides. *Chem. Soc. Rev.* **47**, 6764–6794 (2018).
53. Lin, Z. et al. 2D materials advances: from large scale synthesis and controlled heterostructures to improved characterization techniques, defects and applications. *2D Mater.* **3**, 042001 (2016).
54. Hong, J. et al. Exploring atomic defects in molybdenum disulphide monolayers. *Nat. Commun.* **6**, 1–8 (2015).
55. McDonnell, S., Addou, R., Buie, C., Wallace, R. M. & Hinkle, C. L. Defect-dominated doping and contact resistance in MoS2. *ACS Nano* **8**, 2880–2888 (2014).
56. Li, M. et al. P-type doping in large-area monolayer MoS2 by chemical vapor deposition. *ACS Appl. Mater. Interfac.* **12**, 6276–6282 (2020).
57. Xia, Y. et al. Sulfur-vacancy-enriched MoS2 nanosheets based heterostructures for near-infrared optoelectronic NO2 sensing. *ACS Appl. Nano Mater.* **3**, 665–673 (2019).
58. Ye, G. et al. Defects engineered monolayer MoS2 for improved hydrogen evolution reaction. *Nano Lett.* **16**, 1097–1103 (2016).
59. Zhao, G. Y. et al. Recent Progress on Irradiation-Induced Defect Engineering of Two-Dimensional 2H-MoS2 Few Layers. *Appl. Sci. -Basel* **9**, 53 (2019).
60. Kim, B. H., Gu, H. H. & Yoon, Y. J. Atomic rearrangement of a sputtered MoS2 film from amorphous to a 2D layered structure by electron beam irradiation. *Sci. Rep.* **7**, 11 (2017).
61. Komsa, H. P. et al. Two-Dimensional Transition Metal Dichalcogenides under Electron Irradiation: defect production and doping. *Phys. Rev. Lett.* **109**, 5 (2012).
62. Chang, T. H. P. Proximity effect in electron-beam lithography. *J. Vac. Sci. Technol.* **12**, 1271–1275 (1975).
63. Matsunaga, M. et al. Nanoscale-Barrier Formation Induced by Low-Dose Electron-Beam Exposure in Ultrathin MoS2 Transistors. *ACS Nano* **10**, 9730–9737 (2016).
64. Splendiani, A. et al. Emerging Photoluminescence in Monolayer MoS2. *Nano Lett.* **10**, 1271–1275 (2010).
65. Xie, X. J. et al. Designing artificial 2D crystals with site and size controlled quantum dots. *Sci. Rep.* **7**, 7 (2017).
66. Kang, N. R., Paudel, H. P., Leuenberger, M. N., Tetard, L. & Khondaker, S. I. Photoluminescence Quenching in Single-Layer MoS2 via Oxygen Plasma Treatment. *J. Phys. Chem. C.* **118**, 21258–21263 (2014).
67. Li, H. et al. From Bulk to Monolayer MoS2: evolution of raman scattering. *Adv. Funct. Mater.* **22**, 1385–1390 (2012).
68. Qian, Q. K., Zhang, Z. F. & Chen, K. J. In Situ Resonant Raman Spectroscopy to Monitor the Surface Functionalization of MoS2 and WSe2 for High-k Integration: a first-principles study. *Langmuir* **34**, 2882–2889 (2018).
69. Parkin, W. M. et al. Raman Shifts in Electron-Irradiated Monolayer MoS2. *ACS Nano* **10**, 4134–4142 (2016).
70. Kim, B. H. et al. Effect of sulphur vacancy on geometric and electronic structure of MoS2 induced by molecular hydrogen treatment at room temperature. *RSC Adv.* **3**, 18424–18429 (2013).
71. Wei, X. X. et al. Mo-O bond doping and related-defect assisted enhancement of photoluminescence in monolayer MoS2. *AIP Adv.* **4**, 7 (2014).
72. Turner, N. H. & Single, A. M. Determination of peak positions and areas from wide-scan XPS spectra. *Surf. Interfac. Anal.* **15**, 215–222 (1990).
73. Nefedov, V. I., Firsov, M. N. & Shaplygin, I. S. Electronic-structures of mrho2, mrh2o4, rhmo4 and rh2mo6 on the basis of x-ray spectroscopy and esca data. *J. Electron Spectrosc. Relat. Phenom.* **26**, 65–78 (1982).
74. Barrera, D. et al. Solution synthesis of few-layer 2H MX2 (M = Mo, W; X = S, Se). *J. Mater. Chem. C.* **5**, 2859–2864 (2017).
75. Matsuura, K. et al. Low-Carrier-Density Sputtered MoS2 Film by Vapor-Phase Sulfurization. *J. Electron. Mater.* **47**, 3497–3501 (2018).
76. Shen, T. et al. High mobility monolayer MoS(2)transistors and its charge transport behaviour under E-beam irradiation. *J. Mater. Sci.* **55**, 14315–14325 (2020).
77. Liu, D., Guo, Y., Fang, L. & Robertson, J. Sulfur vacancies in monolayer MoS2 and its electrical contacts. *Appl. Phys. Lett.* **103**, 4 (2013).
78. Leong, W. S. et al. Tuning the threshold voltage of MoS2 field-effect transistors via surface treatment. *Nanoscale* **7**, 10823–10831 (2015).
79. Cho, K. et al. Electrical and Optical Characterization of MoS2 with Sulfur Vacancy Passivation by Treatment with Alkanethiol Molecules. *ACS Nano* **9**, 8044–8053 (2015).
80. Lee, D. et al. Excellent uniformity and reproducible resistance switching characteristics of doped binary metal oxides for non-volatile resistance memory applications. *2006 International Electron Devices Meeting (IEDM)*. 1–4 (2006).
81. Chen, Y. J. et al. Hydrogen induced redox mechanism in amorphous carbon resistive random access memory. *Nanoscale Res. Lett.* **9**, 5 (2014).
82. Liu, C. et al. Two-dimensional materials for next-generation computing technologies. *Nat. Nanotechnol.* **15**, 545–557 (2020).
83. Chen, A. & Lin, M.-R. Variability of resistive switching memories and its impact on crossbar array performance. *2011 International Reliability Physics Symposium (Irps)*. MY. 7.1-MY. 7.4 (2011).
84. Kao, Y. F., Zhuang, W. C., Lin, C. J. & King, Y. C. A Study of the Variability in Contact Resistive Random Access Memory by Stochastic Vacancy Model. *Nanoscale Res. Lett.* **13**, 10 (2018).
85. Le, D., Rawal, T. B. & Rahman, T. S. Single-Layer MoS2 with Sulfur Vacancies: Structure and Catalytic Application. *J. Phys. Chem. C.* **118**, 5346–5351 (2014).
86. Wu, X., Ge, R., Akinwande, D. & Lee, J. C. Understanding of multiple resistance states by current sweeping in MoS2-based non-volatile memory devices. *Nanotechnology* **31**, 465206 (2020).
87. Wu, X. H., Ge, R. J., Huang, Y. F., Akinwande, D. & Lee, J. C. Resistance state evolution under constant electric stress on a MoS2 non-volatile resistive switching device. *RSC Adv.* **10**, 42249–42255 (2020).
88. Chen, C.-Y. et al. RRAM defect modeling and failure analysis based on march test and a novel squeeze-search scheme. *IEEE Trans. Computers* **64**, 180–190 (2014).
89. Zambelli, C., Grossi, A., Olivo, P., Walczyk, C. & Wenger, C. RRAM reliability/performance characterization through array architectures investigations. *2015 IEEE Computer Society Annual Symposium on VLSI*. 327–332 (2015).
90. Chen, Y. Y. et al. Understanding of the endurance failure in scaled HfO 2-based 1T1R RRAM through vacancy mobility degradation. *2012 International Electron Devices Meeting (IEDM)*. 20.23. 21-20.23. 24 (2012).
91. Chen, B. et al. Physical Mechanisms of Endurance Degradation in TMO-RRAM. *2011 International Electron Devices Meeting (IEDM)*. 12.13. 11-12.13. 14 (2011).
92. Yu, S., Guan, X. & Wong, H.-S. P. On the stochastic nature of resistive switching in metal oxide RRAM: Physical modeling, Monte Carlo simulation, and experimental characterization. *2011 International Electron Devices Meeting (IEDM)* 17.13. 11-17.13. 14 (2011).
93. Li, Y. et al. Investigation on the Conductive Filament Growth Dynamics in Resistive Switching Memory via a Universal Monte Carlo Simulator. *Sci. Rep.* **7**, 11 (2017).
94. Choi, H. et al. Nanoscale resistive switching of a copper–carbon-mixed layer for nonvolatile memory applications. *IEEE Electron Device Lett.* **30**, 302–304 (2009).
95. Kim, T.-W. et al. Resistive switching characteristics of polymer non-volatile memory devices in a scalable via-hole structure. *Nanotechnology* **20**, 025201 (2008).
96. Ielmini, D. et al. Scaling analysis of submicrometer nickel-oxide-based resistive switching memory devices. *J. Appl. Phys.* **109**, 034506 (2011).
97. Sahu, D. P., Jetty, P. & Jammalamadaka, S. N. Graphene oxide based synaptic memristor device for neuromorphic computing. *Nanotechnology* **32**, 155701 (2021).
98. Wang, G. et al. Impact of program/erase operation on the performances of oxide-based resistive switching memory. *Nanoscale Res. Lett.* **10**, 1–7 (2015).
99. Kim, M. et al. Zero-static power radio-frequency switches based on MoS2 atomristors. *Nat. Commun.* **9**, 7 (2018).
100. Kim, M. et al. Analogue switches made from boron nitride monolayers for application in 5G and terahertz communication systems. *Nat. Electron.* **3**, 479–485 (2020).

ACKNOWLEDGEMENTS

This work was supported in part by the National Science Foundation (NSF) grant #1809017, and an NSF MRSEC under Cooperative Agreement No. DMR-1720595. The authors acknowledge use of Texas Nanofabrication Facilities supported by the NSF NNCI award #1542159. D.A. acknowledges the Presidential Early Career Award for Scientists and Engineers (PECASE) through the Army Research Office (W911NF-16-1-0277). The authors appreciate Jo Wozniak of Texas Advanced Computing Centre (TACC) for 3D renderings. The authors thank Hugo Celio of Texas Materials Institute (TMI) for XPS measurements.

AUTHOR CONTRIBUTIONS

X.W. and Y.G. contributed equally to this work. X.W., J.L., and D.A. conceived and designed this experiment. Y.G. performed materials transfer, characterization, and device fabrication. R.G. contributed to sample preparation and device fabrication. X.W. carried out DC electrical measurements of 2D non-volatile resistance switching devices. M.I.S. contributed in characterization data analysis and paper preparation. Y.H. conducted the Monte Carlo simulations. All authors contributed to the paper

based on the draft written by X.W., Y.G., J.L., and D.A., J.L., and D.A. coordinated and supervised the research.

COMPETING INTERESTS

The authors declare no competing interests.

ADDITIONAL INFORMATION

Supplementary information The online version contains supplementary material available at https://doi.org/10.1038/s41699-022-00306-8.

Correspondence and requests for materials should be addressed to Jack C. Lee or Deji Akinwande.

Reprints and permission information is available at http://www.nature.com/reprints

Publisher's note Springer Nature remains neutral with regard to jurisdictional claims in published maps and institutional affiliations.